Neuronal Morphology Enhances Robustness to Perturbations of Channel Densities

Yunliang Zang https://orcid.org/0000-0001-8999-1936

Eve Marder http://orcid.org/0000-0001-9632-5448

Volen Center and Department of Biology, Brandeis University, Waltham, MA 02454, USA.

*Corresponding author. Email: marder@brandeis.edu

Abstract

Biological neurons show significant cell-to-cell variability but have the striking ability to maintain their key firing properties in the face of unpredictable perturbations and stochastic noise. Using a population of multi-compartmental models consisting of soma, neurites, and axon for the lateral pyloric (LP) neuron in the crab stomatogastric ganglion, we explored how rebound bursting is preserved when the 14 channel conductances in each model undergo random variations. The soma-axon coupling is critical for the ability of the axon to spike during bursts and consequently determines the set of successful solutions. When the coupling deviates from the biological range, the neuronal tolerance of conductance variations is significantly lessened. This work illustrates that the gross morphological features of these neurons enhance their robustness to perturbations of channel densities and expands the space of individual variability that can maintain a desired output pattern.

Introduction

It is now well-established that multiple sets of maximal conductances of ion channels can produce very similar neuronal activity patterns in both individual neurons and circuits (1-7). Nonetheless, it is also clear that models of desired intrinsic properties are relatively rarely found by just randomly sampling within a space of parameters (6). Thus, it is likely that biological neurons use homeostatic and other developmental mechanisms to successfully find rare sets of values of ion channel conductances that give rise to specific patterns of intrinsic excitability (8-12).

Although single-compartment, isopotential, conductance-based models have been enormously useful in understanding the relationships among ion channels that give rise to electrical excitability, most biological neurons also have complex structures, with differential distributions of channels in the membranes of different neuronal regions. While there are specific examples of conductance-based models of complex neurons (13-15), these models have often been finely tuned to achieve their desired activity patterns, and it is less clear in these more complex models the extent to which complex structures aid or diminish the likelihood of finding vastly different degenerate sets of conductance values that support characteristic activity patterns.

In this study, we exploit a previously developed 4-compartment model of the Lateral Pyloric (LP) neuron of the crustacean stomatogastric ganglion (STG) to look at the influence of LP neuron structure on its robustness to perturbations in its channel densities. This is partly motivated by recent studies that show that the detailed neuropilar projections of the LP neuron have relatively little impact on how slow synaptic events are processed because of the large length constants of the major neurites

(16-18). In this 4-compartment model (soma, axon, and two neurite compartments) only the axon compartment has voltage-gated Na^+ channels, and the segregation of the action potential generating function from those of the synaptic and slow wave functions that is crucial for capturing the specifics of the electrophysiological characteristics of the neuron (6). To create this model Taylor et al (6) generated almost 600,000 randomly selected conductance densities and then sorted them to find ~1,300 models with the desired firing patterns. Most crucially, when isolated, the LP neuron fires tonically, but shows robust rebound bursts in response to inhibitory inputs from its presynaptic partners. These rebound bursts are important in ensuring that the LP neuron fires at an appropriate time during the triphasic pyloric rhythm (19).

The successful ~1,300 models vary considerably in their maximal conductances, and are examples of degenerate or multiple solutions to producing a characteristic behavior. Taylor et al (6) also showed that diverse neuronal properties depend on different sets of membrane conductances, and that these behaviors can be captured by cubic fits of values across neurons. In this paper, we look at the effect of neuronal structure on the robustness of this population of LP neuron models in response to perturbations of conductance densities.

Results

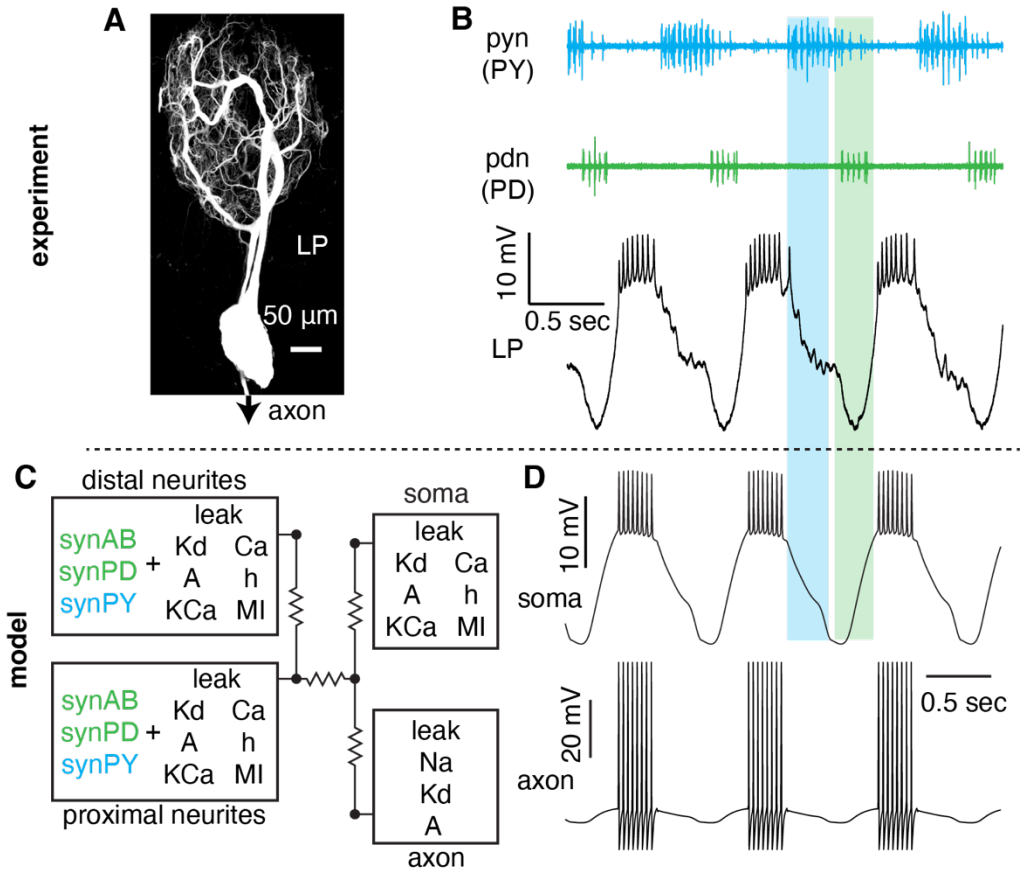

Fig. 1. LP neuron multi-compartment model structure and spike properties. (**A**) A confocal microscopy image of a LP neuron, modified from Fig.2 of (6), Copyright [2009] Society for Neuroscience. (**B**) Extracellular recordings from pyn, pdn and intracellular recording from a PD neuron, from top to bottom, modified from Fig.2 of (6), Copyright [2009] Society for Neuroscience. (**C**) Schematic of the LP neuron models, consisting of an axon, a soma, proximal neurites, and distal neurites with corresponding ion channels and synapses distributed in each compartment, modified from Fig. 1 of (6), Copyright [2009] Society for Neuroscience. (**D**) Example somatic (top) and axonal (bottom) spike waveforms in a model. The blue shading illustrates the timing of the PY neuron inhibition and the green shading illustrates the timing of the PD neuron inhibiton.

Figure 1 shows the basic features of the LP neuron and the model used here (6). A confocal image of a dye-filled LP neuron from the crab, *Cancer borealis*, is seen in Figure 1A. Note the large soma, a single major neurite, many neuropilar branches, and

an axon which exits the STG to travel to innervate the LP neuron's target muscles. The electrophysiological recordings in Figure 1B show the characteristic firing patterns of the LP neuron. The top two traces are extracellular recordings from the pyn (pyloric nerve) and the pdn (pyloric dilator nerve) that show action potentials from the PY (Pyloric) and PD (Pyloric Dilator) neurons. The third trace in Figure 1B is an intracellular recording from the LP neuron, with its sequential inhibition from the PY and PD neurons, followed by the rebound burst in the LP neuron. Significantly, the LP neuron action potentials that ride on the top of the slow wave are not overshooting or undershooting in the soma, but are highly attenuated by the LP neuron's cable. In fact, dual recordings from the soma and the large neurite closer to the axon (20) show that the slow events are almost superimposable although the action potentials are attenuated.

Figure 1C shows the composition of ion channels in each of the 4 compartments in the model. The soma has a leak current (I_{leak}), a modulator current (I_{MI}), three potassium currents (I_{Kd}, delayed-rectifier K^+ current; I_A, A-type K^+ current; I_{KCa}, calcium-activated K^+ current), a calcium current (I_{Ca}), a hyperpolarization inward current (I_h), and three synaptic currents, from the AB (Anterior Burster), PD, and PY neurons synAB, synPD and synPY, respectively. Characteristic waveforms from the LP neuron models are seen in Figure 1D. The top trace is the behavior of the model in the soma compartment, while the bottom trace is the behavior of the model in the axon. The axon generates overshooting action potentials, and only a very small slow wave is visible, while the soma compartment replicates the somatic recordings seen in the biological neurons.

Neuronal Robustness to Channel Conductance Variations

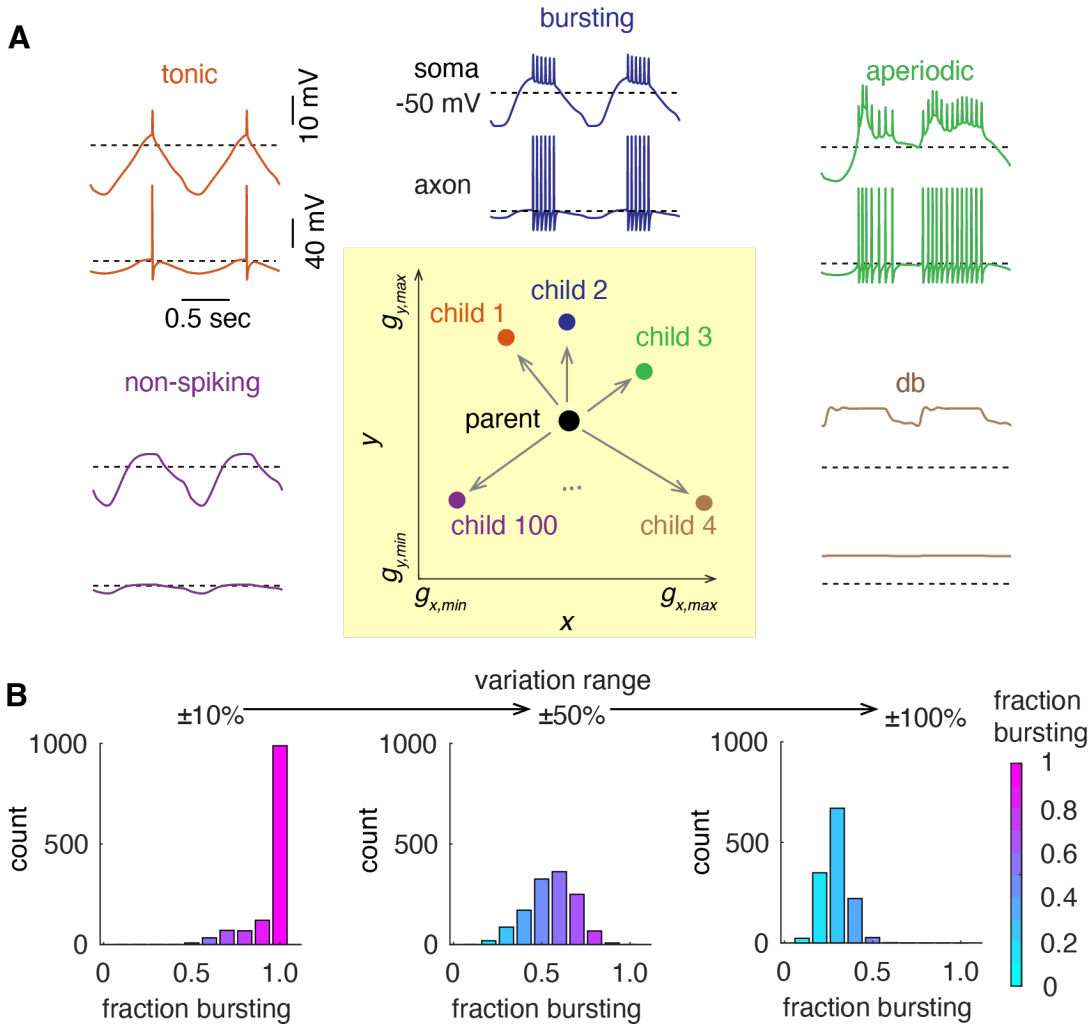

Fig. 2. "Noise" perturbation protocol and neuronal resilience to conductance variations. (**A**) 2-D schematic of the channel conductance perturbation protocol (bottom middle, shaded in yellow). *x* and *y* represent 2 types of ion channels. In each trial, all channel conductances of a "parent" model were simultaneously varied by random values (details in Methods). Each "parent" model (n = 1292) generated new *m* "child" models after *m*-trial perturbations. Example firing patterns in "child" models include tonic spiking (child 1), bursting (child 2), aperiodic spiking (child 3), depolarization block (db, child 4), and non-spiking (child 100). (**B**) Histogram of the ratio of "child" models that are bursters for each "parent" model, when models undergo different ranges of random channel conductance variations, ±10%, ±50%, and ±100% from left to right.

We used 1292 of Taylor's LP neuron models (6), hereafter referred to as "parent" models whose parameters show large cell-to-cell variations despite similar output

patterns. We first varied all of the 14 channel conductances at the same time by different random values in each "parent" model, based on their range of values for all of the 1292 models. Then, for each "parent" model, multiple runs, with different sets of channel perturbations, generated a number of "child" models, which displayed a variety of intrinsic patterns of activity (Fig. 2A; methods).

For all of the "parent" models, the "child" models showed a variety of behaviors, some of which can be generally classified as rebound bursting, tonic spiking, non-spiking, aperiodic spiking, or depolarization block (Fig. 2A). The results of 100 trials for each "parent" model are shown in Figure 2B. For each "parent" model, the ratio of "child" models that are also bursters with at least 2 spikes/burst was calculated to capture its robustness to channel conductance variations. A higher ratio suggests the "parent" model is more robust to channel conductance variations.

When channel conductances were simultaneously varied within ±10% of their corresponding parameter ranges, the rebound bursting pattern was remarkably robust to the conductance variations. For 989 of the "parent" models over 90% of the "child" models generated rebound bursting and for 649 of the "parent" models all the "child" models reliably generated rebound bursting. The overall high ratios of "child" models being bursters indicates that the pattern of rebound bursting is insensitive to the conductance variations in these "parent" models. When channel conductances were varied in larger ranges, more and more "parent" models showed decreased ratios of "child" models being bursters, as reflected by their left-shifted distribution in the histograms (Fig. 2B).

It is always interesting to estimate the size and structure of the 14-dimensional manifold in which these models exist. Previous work on similar conductance-based models argued that models with similar behavior are in connected regions of parameter space (4, 7). For many "parent" models in these previous simulations (n = 649), the perturbation-generated "child" models reliably generate rebound bursting, suggesting that there are reasonable sized areas around those "parent" models with relatively consistent behaviors. We estimate that the size of the manifold in each channel conductance direction is at least 20% of their corresponding conductance ranges.

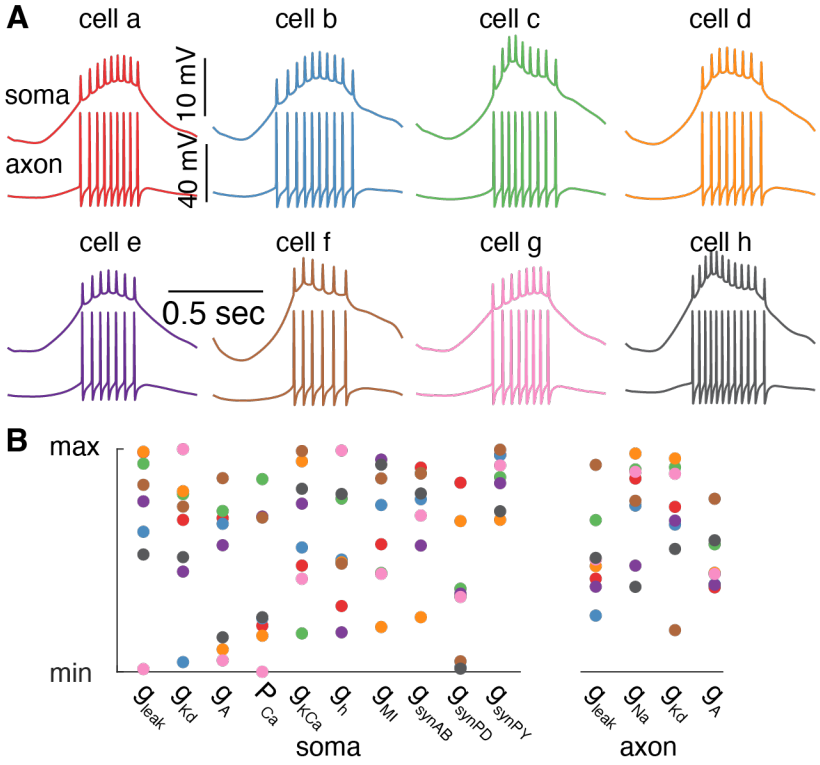

Fig. 3. Robust models are widely distributed in the parameter space. (**A**) The spike waveforms of 8 example "parent" models (models a – h), whose "child" models reliably produce rebound bursting after 10,000-trial perturbations when the variation range is ±10%. (**B**) The parameter distribution of these 8 example models. Colors code different models (models a – h from panel A).

Therefore, we selected 37 elite "parent" models whose "child" models reliably generate rebound bursting for 100 trials of perturbations and have 3 – 11 spikes per burst when the variation range is ±10%. Then, we challenged each of them with 10,000 trials of perturbations. For 23 models, all their "child" models reliably generated rebound bursting and in the other 14 models the lowest ratio of the "child" models generating bursting was 98.95%. These results again support the interpretation that this bursting behavior is relatively insensitive to random channel conductance variations. We plotted the spike waveforms and channel conductances for 8 of the 23 models in Figure 3. Except for larger values of the PY neuron synaptic input, the other channel conductance values spread broadly within their corresponding conductance ranges, suggesting that robust models exist widely in the 14-dimension parameter space.

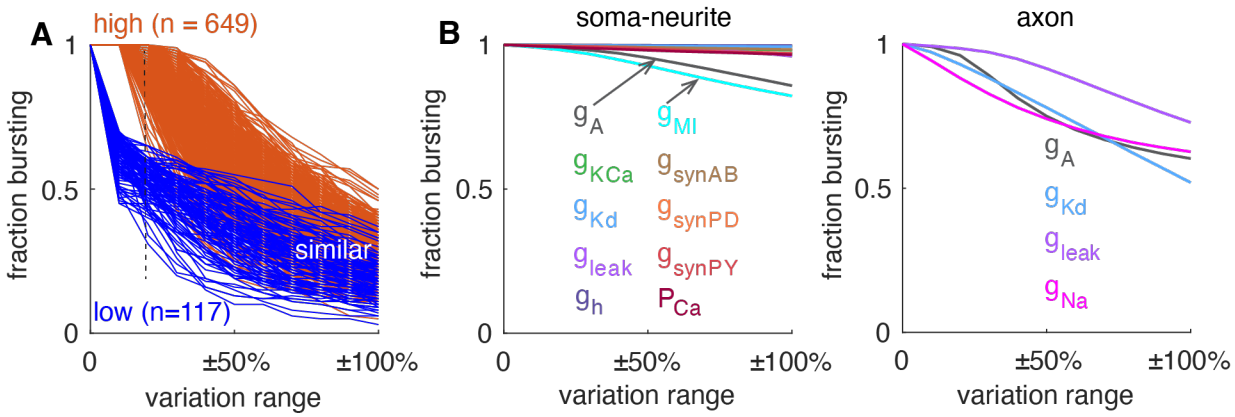

Fig. 4. Factors regulating neuronal robustness. (**A**) The effect of variation range on neuronal resilience between two groups of neurons that have high (100%, orange) and low (<70%, blue) ratio of "child" models that are bursters when the variation range is ±10%. (**B**) The sensitivity of neuronal resilience to individual channel conductance variations (coded by colors). Left and right plots show the effect of varying one of the channel conductances in the soma-neurite and the axon, respectively. The x axis represents conductance variation range, and the y axis represents the average ratio of "child" models that are bursters.

If one group of neurons shows an advantage in maintaining rebound bursting relative to another group within a small variation range, is this advantage preserved with larger variations? When the variation range increases, the two groups of neurons gradually have similar ratios of maintaining the bursting pattern regardless of their ratios with smaller variation ranges (Fig. 4A).

We also explored how the effect of varying individual channel conductance variations on the robustness of rebound bursting. Compared to the effect of varying 14 channel conductances simultaneously, the models are more resilient to single-channel conductance variations. In the soma and neurites, the model's performance just slightly shows sensitivity to I_A and I_{MI} conductances. In contrast, varying each of the conductances in the axon changes the model's firing pattern more efficiently.

The Effect of Soma-axon Coupling on Axonal Spiking during Bursts

In the LP neuron, the soma and neurites generate rebound slow waves, that propagate to evoke bursts of Na^+ spikes in the axon. Therefore, the soma-axon coupling is key to regulating the bursts of spikes. In the whole model database (n = 1292), we varied the axial resistivity, Ra, between the soma and the axon to change their degree of coupling, while the Ra values in other compartments were fixed at the control value of 100 Ωcm.

When the soma to axon Ra was changed, some models no longer produced rebound bursts (Fig. 5A). All models generated rebound bursting when the Ra was in the range of 95 Ωcm – 125 Ωcm (Fig. 5B). For Ra in the range of 40 Ωcm – 300 Ωcm, 1175 (91%) models generated rebound bursting. These results suggest that the bursting

pattern is resilient to Ra changes around the control value of 100 Ωcm. When Ra deviated considerably from the control value, the number of rebound bursting neurons decreased significantly. The models that generate rebound bursting with larger Ra

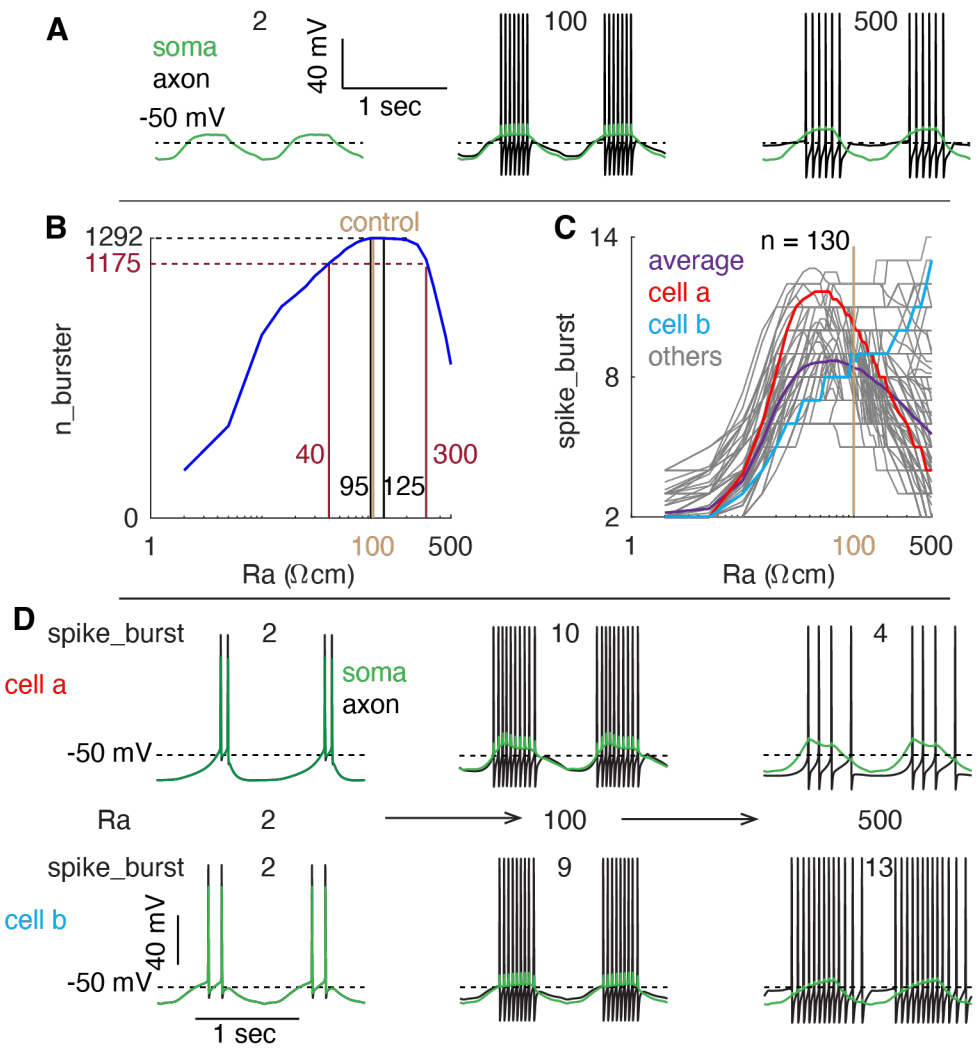

Fig. 5. The effect of soma-axon coupling. (**A**) Example somatic (green) and axonal (black) spike waveforms when Ra was changed from 100 Ωcm (middle) to 2 Ωcm (left) and 500 Ωcm (right). (**B**) The relationship between the soma to axon Ra and the bursting neuron population size (n_burster). n = 1292 when Ra = 100 Ωcm under control condition. (**C**) The relationship between the soma to axon Ra and the number of spikes per burst (spike_burst) in neurons that generate rebound bursting regardless of Ra changes (n = 130). Purple, population average; red and cyan, two example neurons; gray, other neurons. (**D**) The effect of soma to axon Ra on somatic (green) and axonal (black) bursting changes in the example cells (cells a and b) highlighted in C (Ra, 2 Ωcm

→ 500 Ωcm from left to right). In all simulations, there are no channel conductance variations.

deviations are usually bursters when the Ra deviation is lower. For example, in the range of 2 Ωcm – 100 Ωcm, if a model is a burster with a smaller Ra, it is always a burster when the Ra has a larger value, with rare exceptions for the Ra from 15 Ωcm to 20 Ω cm (2 exceptions) and from 35 Ωcm to 40 Ωcm (1 exception).

The simulation results above show that the degree of soma-axon coupling affects the number of bursting neurons. We selected 130 models that always generate the pattern of rebound bursting for the Ra within the tested range of 2 Ωcm – 500 Ωcm. The number of spikes per burst reflects the ability of the axon to spike during bursts. For most of these neurons, the number of spikes per burst shows biphasic changes with the Ra value, as also reflected by the average changes (Fig. 5D). However, in several neuron models, this number monotonically increases within the tested Ra range. When the Ra value is small, the soma and the axon approach are almost isopotential, as revealed by the nearly overlapped somatic and axonal membrane potentials (Fig. 5D, left).

When the soma and axon are strongly coupled, this reduces the ability of the axon to spike during bursts for two reasons. First, the axonal membrane potential after each spike is closer to the somatic slow-wave peak (bottom Vm during the bursts), which reduces the recovery of Na^+ channels from inactivation. Second, the soma exerts a larger capacitance load on the axon during spiking (top Vm during the bursts). Therefore, when the Ra was 2 Ωcm, the number of spikes per burst was low. Increasing Ra to make the soma and the axon more isolated should increase the axonal ability to spike during bursts if just considering the above 2 factors. However, the larger isolation between the

soma and the axon also reduces the axial current from the somatic slow wave that triggers axonal spiking during bursts. Consequently, changes in the number of spikes per burst depend on the balance of the 3 factors when the Ra value changes (Fig. 5D).

The Effect of Soma-axon Coupling on Neuronal Robustness

We first explored how soma-axon coupling affects neuronal robustness for all the 1292 "parent" models. When Ra is near the control value of 100 Ωcm, the average ratios of "child" models being bursters are insensitive to Ra changes irrespective of conductance variation ranges (Fig. 6A1, Ra = 50, 100 and 125 Ωcm). However, when the soma-axon coupling gets too strong (Ra = 2 Ωcm) or too weak (Ra = 500 Ωcm), the average ratios of "child" models being bursters are significantly reduced. Under these conditions, for many "parent" models that lose the pattern of rebound bursting, their "child" models become bursters when the channel conductances are perturbed to appropriate ranges (Fig. 6A2, A3).

When Ra is 2 Ωcm, the average ratio of "child" models being bursters shows biphasic changes. Under these conditions, some of the original "parent" models are no bursting neurons, but neighboring parameter space may remain bursting (Fig. 6A2, A3). The "density" of bursting neuron models in the whole parameter space is nearly unchanged when Ra is near 100 Ωcm but significantly decreases when the Ra deviates further from the control value.

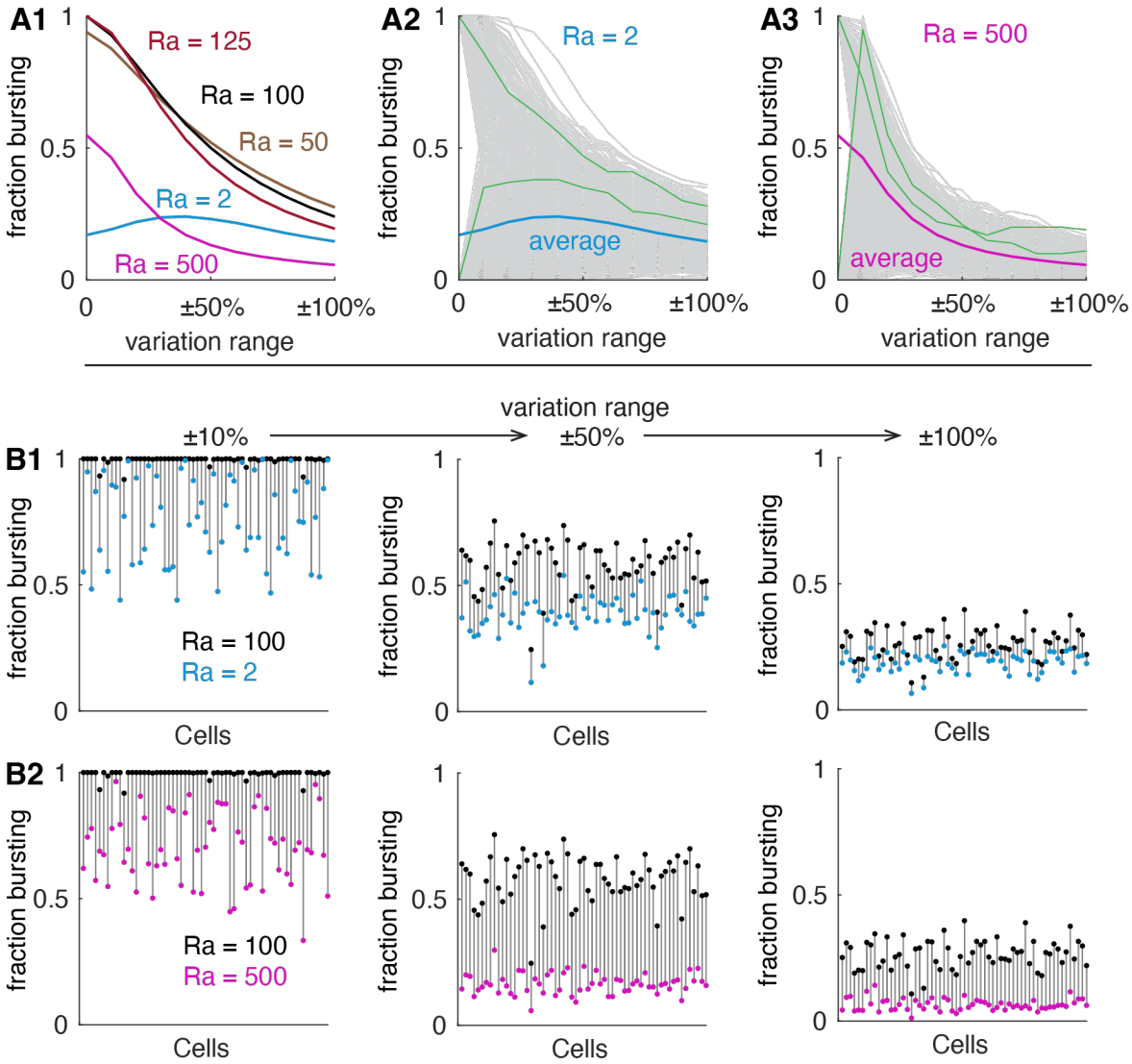

Fig. 6. The effect of soma-axon coupling on neuronal resilience to conductance variations. (**A**) The effect of soma to axon Ra on neuronal resilience to conductance variations for all the "parent" models. A1, The population average ratio of "child" models that are bursters with different Ra values (coded by colors). A2 and A3 show individual neuronal ratios of "child" models that are bursters for Ra = 2 Ωcm and 500 Ωcm, respectively. Green traces show typical example plots. Blue and magenta traces show population average ratios, as in A1. Gray traces show other individual neurons. (**B**) The comparison of each neuronal ratios of "child" models that are bursters when Ra is changed from the control value of 100 Ωcm. B1, Ra is changed from 100 Ωcm (black dots) to 2 Ωcm (blue dots); B2, Ra is changed from 100 Ωcm (black dots) to 500 Ωcm (magenta dots). From left to right, conductance variation range increases from ±10% to ±100%. 80 of the total 131 elite "parent" models were shown.

To explore how the degree of soma-axon coupling affects the ability of individual neurons to maintain rebound bursting when faced with channel conductance variations, we selected 131 elite models from the 1292 "parent" models. These 131 elite "parent" models reliably generate rebound bursting when the Ra is 2 Ωcm, 100 Ωcm, and 500 Ωcm. Strikingly, for each of these "parent" models, the ratio of "child" models that are bursters consistently decreases when Ra is changed from 100 Ωcm to 2 Ωcm and from 100 Ωcm to 500 Ωcm (Fig. 6B, only 80 cells were plotted, but all cells show the same trend), regardless of the conductance variation ranges. These simulation results suggest that the degree of soma-axon coupling determines the size of the manifold that corresponds to bursting neurons and therefore the neuronal robustness to channel conductance variations.

Discussion

Most neurons have complex structures over which ion channel distributions must be established such that the neuron's characteristic electrical properties are maintained, given the inevitable "noise" that must accompany the ongoing turnover of channels in the membrane. It is known that some neuronal types display specific patterns of channel distributions that are thought to aid in the neuronal computations that these neurons perform (21-23). Therefore, it becomes important to determine the extent to which the three-dimensional structure of neurons makes them more or less sensitive to fluctuations in channel densities across the structures.

In this work, we used a population of LP neuron compartmental models developed previously (6) to explore neuronal robustness to channel conductance variations. All members of this population met a series of criteria that ensured that they

capture many of the essential features of the biological neurons whose behavior they were intended to capture (6). At the same time, these models show considerable degeneracy in that the specific values of their conductances were highly variable (6). While these models separate the soma, axon, and dendritic compartments, and are therefore more biologically "realistic" than single compartment, point, neurons, they are not intended to capture all of the detailed structures of individual STG neurons.

In models of one or two dimensions, it is easy to find the parameter sets that define the boundary between different types of neuronal activity patterns (24, 25). However, as the number of dimensions increases, it becomes more challenging to characterize the parameter space for neurons with specific properties (7, 14). For the 14-dimension parameter space here, it would be a daunting task to locate all possible bursting models with a grid search, because it is impossible to know whether the sampling step size is small enough (4). Instead, we used random parameter perturbations, which does not provide an unambiguous map of the entire manifold. Nonetheless, if all "child" models are bursters after exerting random and simultaneous conductance perturbations for sufficiently many trials, it argues the existence of a multi-dimensional manifold that contains the very large majority of models of similar behavior (7). We did this in a subset of neuron models for 10,000 trials and most of them reliably generated rebound bursting after perturbations (Fig. 3).

Multiple mechanisms likely exist that can allow neurons to compensate for perturbation-caused changes. In homeostatic models of intrinsic excitability and regulation of synaptic strength, both ion channel conductances and synaptic strength can be altered to recover neuronal and circuit function properties in response to

deviations from a set-point (12, 26-30). Some homeostatic mechanisms require new protein synthesis, and therefore recovery may be slow and require hours or even days, whereas other processes may be more rapid (28, 30-32).

Neurons constantly face diverse perturbations such as temperature changes, neuromodulation, and stochastic changes in protein synthesis, but they rarely fail in healthy animals under physiological conditions. This argues that most neurons are not sitting too close to bifurcations, but can tolerate some changes in their parameters without loss of function.

The effect of morphology on the stability of physiological activity has received less attention than it probably merits. Nonetheless, there are examples of structural alterations that can be homeostatically regulated to control activity (33).

In many neurons, including those of the STG, neuronal Na^+ spikes are initiated in the axon. In STG neurons, the slow waves that underlie bursting depend on channels in the soma and major neurites, and synaptic inputs and outputs occur on the processes, and these various regions of the neuron are coupled appropriately (6). Biological ranges of soma-axon coupling can increase the density and the size of manifolds that allow rebound bursting (Figs. 5, 6). Recent data argue that the detailed morphology of STG neurons are not important for their overall function (16-18). Thus, instead of requiring the detailed specification of the number and location of each ion channel, this strategy requires only the specification of a generic structure, that in turn depends on an appropriate range of values of the electrical coupling between the soma and axon. The control value of 100 Ωcm for the Ra in this model falls in the middle range of the experimentally reported values (34) and was originally chosen to make the spike

amplitudes on top of somatic slow waves match experimental data (6). While individual LP and other STG neurons show substantial animal to animal variability in channel conductance densities and channel mRNAs (2, 35-40), it is important to remember that the motor patterns produced by these neurons in the pyloric circuit is tightly maintained, and the LP neuron's rebound burst is critical for its proper function (19).

The findings in this work amplify those of the sloppy morphology observed in crab stomatogastric ganglion neurons (16-18). Although the morphological structures of these neurons exhibit significant cell-to-cell variations, they are electrotonically compact by gradually tapering neurites from the soma to the distal tips. This elegant, but not too rigid, solution makes graded transmission resilient to electrotonic decrement across sparsely distributed, synchronous presynaptic sites. Previously we argued that the separation of synaptic integration and slow waves from axonal spike initiation zones may be a morphological strategy established to avoid shunting of synaptic currents. Here, we show that this division of labor can also make neurons more robust to perturbations.

The findings in this study may also be relevant to other neuronal systems, given the fact that spike bursts are widely observed in the cerebellum (41, 42), the neocortex (43), and the hippocampus (44). For example, the inferior olive neurons in the cerebellum show significant similarities to the LP neuron. Inferior olive neurons show subthreshold oscillations in the soma and then trigger axonal spike bursts to guide cerebellum-related movement and learning (41). Additionally, soma-axon coupling is also critical for the initiation of axonal spike bursts (complex spikes) in cerebellar Purkinje cells (13, 45). Because of the functional importance of these signals in

cerebellar coding and learning, the reliability of triggering the axonal bursting signals determines the robustness of corresponding behavioral functions. Furthermore, not limited to the effect of soma-axon coupling and the pattern of spike bursting, neurons may utilize their intact structure in cooperation with ion channels to maintain a robust functional output in other spiking patterns (46, 47).

Methods

We used the LP neuron multicompartment models constructed previously (6) and implemented them in NEURON 7.6 (48). These models were constructed to replicate the rebound bursting properties observed in the LP neuron of the crab stomatogastric ganglion. The LP neuron receives synaptic inhibition from AB, PD, and PY neurons. The inhibitory inputs trigger rebound slow waves in the neurites and the soma, which propagate to the axon to trigger Na^+ spike bursts. In this work, we adopted 1292 out of the original 1304 cell models. The excluded cell models either need a long time to generate rebound bursting or even don't generate this pattern after reaching a steady state, possibly because of NEURON version changes. In this work, we explored how the rebound bursting pattern is preserved when the models undergo random ion channel conductance variations. The channel types and compartmental distributions are shown in Fig. 1. More detailed current formulations can be found in the original work (6). For conductance perturbation simulations within a variation range, all the 14 channel conductances were simultaneously and independently varied by values randomly sampled in the range of [-1, +1]*variation_range*($g_{x,max}$ - $g_{x,min}$). x represents a type of ionic current; $g_{x,max}$ and $g_{x,min}$ represent the maximum and the minimum conductances of current x in the whole parameter space, respectively. A conductance was set to 0 if the value became negative after a random perturbation. A "child" model was classified as a burster if there were at least 2 spikes per burst. For the elite "parent" models in Fig. 3, the first criterion is all their "child" models need to be bursters when the variation range is ±10%. The second criterion is the number of spikes per burst in the "parent" models and their corresponding "child" models need to be in the range of 3 – 11, although other numbers have also been observed in experiments (6). For results in Figs. 5 and 6, only

the axial resistivity Ra between the soma and the axon was varied to simulate different degrees of soma-axon coupling. When the Ra decreases, the soma and axon become more coupled and approach to be isopotential. When the Ra increases, the soma and axon become more isolated. We constrained the Ra within the range of 2 Ωcm – 500 Ωcm, because we wanted to maintain a number of neurons in Fig. 5C and Fig. 6B to compare the changes in individual neurons.

Acknowledgement

This work was supported by NIH Grants R35NS097343 and R01MH046742.

References

1. L. M. Alonso, E. Marder, Visualization of currents in neural models with similar behavior and different conductance densities. *Elife* **8**, e42722 (2019).
2. M. S. Goldman, J. Golowasch, E. Marder, L. F. Abbott, Global structure, robustness, and modulation of neuronal models. *J. Neurosci.* **21**, 5229-5238 (2001).
3. J. Golowasch, M. S. Goldman, L. F. Abbott, E. Marder, Failure of averaging in the construction of a conductance-based neuron model. *J. Neurophysiol.* **87**, 1129-1131 (2002).
4. A. A. Prinz, C. P. Billimoria, E. Marder, Alternative to hand-tuning conductance-based models: construction and analysis of databases of model neurons. *J. Neurophysiol.* **90**, 3998-4015 (2003).
5. A. A. Prinz, D. Bucher, E. Marder, Similar network activity from disparate circuit parameters. *Nat. Neurosci.* **7**, 1345-1352 (2004).
6. A. L. Taylor, J. M. Goaillard, E. Marder, How multiple conductances determine electrophysiological properties in a multicompartment model. *J. Neurosci.* **29**, 5573-5586 (2009).

7. A. L. Taylor, T. J. Hickey, A. A. Prinz, E. Marder, Structure and visualization of high-dimensional conductance spaces. *J. Neurophysiol.* **96**, 891-905 (2006).

8. S. Gorur-Shandilya, E. Marder, T. O'Leary, Activity-dependent compensation of cell size is vulnerable to targeted deletion of ion channels. *Sci. Rep.* **10**, 15989 (2020).

9. G. LeMasson, E. Marder, L. F. Abbott, Activity-dependent regulation of conductances in model neurons. *Science* **259**, 1915-1917 (1993).

10. Z. Liu, J. Golowasch, E. Marder, L. F. Abbott, A model neuron with activity-dependent conductances regulated by multiple calcium sensors. *J. Neurosci.* **18**, 2309-2320 (1998).

11. T. O'Leary, A. H. Williams, J. S. Caplan, E. Marder, Correlations in ion channel expression emerge from homeostatic tuning rules. *Proc. Natl. Acad. Sci. U. S. A.* **110**, E2645-2654 (2013).

12. T. O'Leary, A. H. Williams, A. Franci, E. Marder, Cell types, network homeostasis, and pathological compensation from a biologically plausible ion channel expression model. *Neuron* **82**, 809-821 (2014).

13. Y. Zang, S. Dieudonne, E. De Schutter, Voltage- and Branch-Specific Climbing Fiber Responses in Purkinje Cells. *Cell. Rep.* **24**, 1536-1549 (2018).

14. P. Achard, E. De Schutter, Complex parameter landscape for a complex neuron model. *PLoS. Comput. Biol.* **2**, e94 (2006).

15. Y. Zang, S. Hong, E. De Schutter, Firing rate-dependent phase responses of Purkinje cells support transient oscillations. *Elife* **9**, e60692 (2020).

16. A. G. Otopalik *et al.*, Sloppy morphological tuning in identified neurons of the crustacean stomatogastric ganglion. *Elife* **6**, e22352 (2017).

17. A. G. Otopalik, A. C. Sutton, M. Banghart, E. Marder, When complex neuronal structures may not matter. *Elife* **6**, e23508 (2017).

18. A. G. Otopalik, J. Pipkin, E. Marder, Neuronal morphologies built for reliable physiology in a rhythmic motor circuit. *Elife* **8**, e41728 (2019).

19. D. K. Hartline, D. V. Gassie, Jr., Pattern generation in the lobster (Panulirus) stomatogastric ganglion. I. Pyloric neuron kinetics and synaptic interactions. *Biol. Cybern.* **33**, 209-222 (1979).

20. J. Golowasch, E. Marder, Ionic currents of the lateral pyloric neuron of the stomatogastric ganglion of the crab. *J. Neurophysiol.* **67**, 318-331 (1992).

21. J. Magee, D. Hoffman, C. Colbert, D. Johnston, Electrical and calcium signaling in dendrites of hippocampal pyramidal neurons. *Annu. Rev. Physiol.* **60**, 327-346 (1998).

22. J. C. Magee, Dendritic hyperpolarization-activated currents modify the integrative properties of hippocampal CA1 pyramidal neurons. *J. Neurosci.* **18**, 7613-7624 (1998).

23. J. C. Magee, M. Carruth, Dendritic voltage-gated ion channels regulate the action potential firing mode of hippocampal CA1 pyramidal neurons. *J. Neurophysiol.* **82**, 1895-1901 (1999).

24. G. Drion, T. O'Leary, E. Marder, Ion channel degeneracy enables robust and tunable neuronal firing rates. *Proc. Natl. Acad. Sci. U. S. A.* **112**, E5361-5370 (2015).

25. H. Ori, E. Marder, S. Marom, Cellular function given parametric variation in the Hodgkin and Huxley model of excitability. *Proc. Natl. Acad. Sci. U. S. A.* **115**, E8211-E8218 (2018).

26. J. Cannon, P. Miller, Synaptic and intrinsic homeostasis cooperate to optimize single neuron response properties and tune integrator circuits. *J. Neurophysiol.* **116**, 2004-2022 (2016).

27. J. Cannon, P. Miller, Stable Control of Firing Rate Mean and Variance by Dual Homeostatic Mechanisms. *J Math Neurosci* **7**, 1 (2017).

28. G. W. Davis, Homeostatic control of neural activity: from phenomenology to molecular design. *Annu. Rev. Neurosci.* **29**, 307-323 (2006).

29. G. Turrigiano, Too many cooks? Intrinsic and synaptic homeostatic mechanisms in cortical circuit refinement. *Annu. Rev. Neurosci.* **34**, 89-103 (2011).

30. G. G. Turrigiano, The dialectic of Hebb and homeostasis. *Philos. Trans. R. Soc. Lond. B. Biol. Sci.* **372**, 20160258 (2017).

31. R. Gowrishankar *et al.*, Region-Specific Regulation of Presynaptic Dopamine Homeostasis by D2 Autoreceptors Shapes the In Vivo Impact of the Neuropsychiatric Disease-Associated DAT Variant Val559. *J. Neurosci.* **38**, 5302-5312 (2018).

32. Y. Kulik, R. Jones, A. J. Moughamian, J. Whippen, G. W. Davis, Dual separable feedback systems govern firing rate homeostasis. *Elife* **8**, e45717 (2019).

33. M. S. Grubb, J. Burrone, Activity-dependent relocation of the axon initial segment fine-tunes neuronal excitability. *Nature* **465**, 1070-1074 (2010).

34. A. Roth, M. Hausser, Compartmental models of rat cerebellar Purkinje cells based on simultaneous somatic and dendritic patch-clamp recordings. *J. Physiol.* **535**, 445-472 (2001).

35. J. M. Goaillard, A. L. Taylor, D. J. Schulz, E. Marder, Functional consequences of animal-to-animal variation in circuit parameters. *Nat. Neurosci.* **12**, 1424-1430 (2009).

36. J. Golowasch, L. F. Abbott, E. Marder, Activity-dependent regulation of potassium currents in an identified neuron of the stomatogastric ganglion of the crab Cancer borealis. *J. Neurosci.* **19**, RC33 (1999).

37. A. J. Northcutt *et al.*, Molecular profiling of single neurons of known identity in two ganglia from the crab Cancer borealis. *Proc. Natl. Acad. Sci. U. S. A.* **116**, 26980-26990 (2019).

38. A. J. Northcutt *et al.*, Deep sequencing of transcriptomes from the nervous systems of two decapod crustaceans to characterize genes important for neural circuit function and modulation. *BMC. Genomics.* **17**, 868 (2016).

39. D. J. Schulz, J. M. Goaillard, E. Marder, Variable channel expression in identified single and electrically coupled neurons in different animals. *Nat. Neurosci.* **9**, 356-362 (2006).

40. D. J. Schulz, J. M. Goaillard, E. E. Marder, Quantitative expression profiling of identified neurons reveals cell-specific constraints on highly variable levels of gene expression. *Proc. Natl. Acad. Sci. U. S. A.* **104**, 13187-13191 (2007).

41. A. Mathy *et al.*, Encoding of oscillations by axonal bursts in inferior olive neurons. *Neuron* **62**, 388-399 (2009).

42. Y. Zang, E. De Schutter, Climbing Fibers Provide Graded Error Signals in Cerebellar Learning. *Front. Syst. Neurosci.* **13**, 46 (2019).

43. M. E. Larkum, J. J. Zhu, B. Sakmann, A new cellular mechanism for coupling inputs arriving at different cortical layers. *Nature* **398**, 338-341 (1999).

44. H. Su, G. Alroy, E. D. Kirson, Y. Yaari, Extracellular calcium modulates persistent sodium current-dependent burst-firing in hippocampal pyramidal neurons. *J. Neurosci.* **21**, 4173-4182 (2001).

45. J. T. Davie, B. A. Clark, M. Hausser, The origin of the complex spike in cerebellar Purkinje cells. *J. Neurosci.* **28**, 7599-7609 (2008).

46. E. Hay, F. Schurmann, H. Markram, I. Segev, Preserving axosomatic spiking features despite diverse dendritic morphology. *J. Neurophysiol.* **109**, 2972-2981 (2013).

47. M. S. Hamada, S. Goethals, S. I. de Vries, R. Brette, M. H. Kole, Covariation of axon initial segment location and dendritic tree normalizes the somatic action potential. *Proc. Natl. Acad. Sci. U. S. A.* **113**, 14841-14846 (2016).

48. M. L. Hines, N. T. Carnevale, The NEURON simulation environment. *Neural. Comput.* **9**, 1179-1209 (1997).